Radiation Measurements 198 (2026) 107806

Contents lists available at ScienceDirect

Radiation Measurements

journal homepage: www.elsevier.com/locate/radmeas

Application of LiF fluorescent nuclear track detectors for measurements of cosmic radiation at the lunar orbit within the MARE experiment

P. Bilski [a,*], A. Kilian [a], M. Sankowska [a], T. Horwacik [a], T. Berger [b]

[a] Institute of Nuclear Physics, Polish Academy of Sciences, IFJ PAN, Krakow, PL-31-342, Poland
[b] Institute of Aerospace Medicine, German Aerospace Center, DLR, Cologne, 51147, Germany

ABSTRACT

A method for reconstructing linear energy transfer (LET) fluence spectra of a complex cosmic radiation field using LiF-based fluorescent nuclear track detectors (FNTD) was developed. It is based on the relationship between track intensity and LET and includes corrections for the particle's angle of incidence. The method was successfully applied to the analysis of the detectors exposed to radiation at lunar orbit in the frame of the MARE project (part of the NASA Artemis I mission).

The obtained spectra were compared with the data from etched plastic nuclear track detectors (PNTD), which were located in the same places as FNTDs. The spectra measured with both detector systems agreed, with the exception of $LET_{H2O} > 100$ keV/μm, where FNTD overestimated the PNTD. This, in turn, caused overestimation of the dose (by up to 30%) and quality factor (by about 15%). When calculations were restricted to $LET_{H2O} < 100$ keV/μm, the agreement was within 15% for dose and within a few percent for quality factor.

1. Introduction

The method of fluorescent imaging of the tracks produced by charged nuclear particles was originally developed with C- and Mg-doped aluminium oxide crystals, and the detectors used for this purpose were named Fluorescent Nuclear Track Detectors (FNTDs) (Akselrod et al., 2006; Akselrod and Kouwenberg, 2018; Akselrod and Sykora, 2011). The physical principle of the method is based on the photoluminescence of the colour centres created by ionizing particles on their path through a crystal, which can be observed with a fluorescent microscope under high magnification.

During the last decade, FNTDs based on another material, namely lithium fluoride (LiF) crystals, were developed (Bilski and Marczewska, 2017). Similarly to Al_2O_3:C,Mg, they can register tracks of all densely ionizing particles. LiF FNTDs have been shown to be suitable for applications such as alpha particle spectrometry, proton beam characterization, and neutron dosimetry (Bilski et al., 2020, 2024a; Sankowska et al., 2024).

Cosmic radiation in space is a radiation field consisting mainly of densely ionizing particles. For decades, another type of track detector, namely chemically etched plastic nuclear track detectors (PNTDs) has been, in combination with thermoluminescent detectors (TLD), the standard method of passive dosimetry during spaceflights (Benton and Benton, 2001). In this type of detector, the latent tracks created by charged particles are enlarged and brought into observation by applying chemical treatment (etching). The main advantage of PNTDs is their ability to measure the linear energy transfer (LET) fluence spectrum of a complex radiation field, and subsequently calculate the radiation quality factor, Q, thereby enabling, in combination with the TLDs, to determine the full absorbed dose and dose equivalent.

In the case of FNTDs, while it has been demonstrated that they are capable of providing some information about LET, there have been no attempts to date to use them for determining the cosmic radiation LET spectrum. The present work aims to address this gap.

In year 2022, the research team of the IFJ PAN in Kraków took part in the Matroshka AstroRad Radiation Experiment (MARE) in the frame of the NASA Artemis I mission to the Moon orbit (see section 2.5 for details) (Berger, 2023; Bilski et al., 2024b). The experiment consisted of exposure of two human phantoms equipped with various detector systems provided by several collaborating teams. Our main research tools in this experiment were thermoluminescent detectors (TLD) and track-etched detectors, however, MARE also provided an opportunity to investigate the performance of the newly developed LiF FNTDs in this specific radiation field.

The motivation behind the present work was therefore developing a methodology for analysing fluorescent tracks created by cosmic radiation, with the aim of extracting information on ionization density from the tracks. The ultimate goal was to reconstruct LET fluence spectra from track parameters in a manner similar to that used with track-etched detectors (which acted as reference detectors in this work).

* Corresponding author.
E-mail address: pawel.bilski@ifj.edu.pl (P. Bilski).

https://doi.org/10.1016/j.radmeas.2026.107806
Received 1 April 2026; Received in revised form 18 August 2026; Accepted 1 September 2026
Available online 1 September 2026

2. Materials and methods

2.1. FNTD preparation

LiF single crystals were grown using the Czochralski method at the IFJ PAN. Two types of crystals were produced: one with the natural Li isotopic composition and the other with Li highly enriched with ^{7}Li. The latter were needed to minimize the effect of (n,α) reactions involving ^{6}Li nuclei, which produce a number of α and Triton tracks that may be misinterpreted as originating from cosmic-ray ions, and which will be seen in space due to the creation of a secondary neutron field due to the interaction of the galactic cosmic rays with the hull of a spacecraft. Powdered LiF, which was used as a starting material for crystal growth, was also synthesized at the IFJ PAN. Details of the chemical procedure and crystal growth can be found elsewhere (Sankowska et al., 2024).

The grown crystals were cut with diamond saws into transparent square plates typically measuring about 3 × 3 × 1 mm^3 and then polished with fine abrasive strips and rinsed in acetone. Subsequently, the crystal samples were heated to a temperature close to the LiF melting point (820–830 °C) for 10 min. This treatment improved the quality of the crystal surface by removing small scratches left by polishing.

2.2. FNTD microscopic observations and image analysis

Microscopic observations were performed using a Nikon Eclipse Ni wide-field microscope with a DS Qi2 camera. A pE-100 440 nm LED light source (CoolLED) together with a band-pass filter (ET445/30) was used for illumination. A long-pass filter (ET570LP) was used for emission light. All images were acquired using a 100× TU Plan ELWD objective lens (NA 0.80). The resulting field of view had a diameter of approximately 95 μm (an observed area of around 7500 μm^2). Due to technical limitations, making precise localisation of subsequent fields of view on the crystal impossible, we were able to scan only about 80 fields per detector.

The recorded data consisted of stacks, i.e. series of images registered with the focus set at different focal depths within the crystal taken in 1-μm steps. The acquisition time for each image was 20 s, which was the longest time required to avoid saturating the high-LET tracks. Typically, the first image was taken at 5 μm below the crystal surface and the whole stack consisted of 20 layers. All images were 14-bit greyscale with a resolution of 13.7 pixels per micrometre, and they were stored in the Nikon ND2 file format. The analyses of the images were carried out using ImageJ/Fiji software (Schindelin et al., 2012). Since the signal from the weakest tracks exceeded the background level by only about 20%, the accurate subtraction of the background was crucial for the analysis. Therefore, as a first step, the background signal was removed from the images by applying a self-developed *BackgrondRemover* plugin to ImageJ (Kilian et al., 2025). Further analyses were also performed using ImageJ software. For each track having a linear shape (see section 2.3 for explanation) two parameters were determined: maximum track intensity divided by acquisition time and angle of incidence. The first parameter was earlier found to be the most reliable and robust for establishing a relationship with LET (Bilski et al., 2024a). The incidence angle (marked β in Fig. 3) is defined here as the zenith angle, i.e., the angle between the incident direction and the surface normal of the crystal. The incidence angle ranges from 0° to 90°, with 0° corresponding to an incident direction perpendicular to the crystal surface and 90° corresponding to an incident direction parallel to the crystal surface.

2.3. Structure and geometry of FNTD tracks

An important feature of fluorescent tracks is that the intensity of fluorescence varies along the tracks. These fluctuations can cause the intensity to drop below the level of background noise. For tracks of densely ionizing particles, this results in breaks in a track (Fig. 1a), whereas for low-LET particles, the tracks consist of a series of bright spots only (Fig. 1b).

Fig. 1 shows the tracks of particles that were directed nearly parallel to the detector surface. In a general case, when a particle is directed under an angle to the detector, at a given depth only a part of the track is in focus, as illustrated in Fig. 2. By projecting the brightest pixels of all layers onto the XY plane, the so-called maximum intensity projection (MIP) is obtained, which reconstructs the linearly-shaped tracks (Figs. 2h and 3a). It should, however, be noted, that in the case of low-LET particles, with sparsely distributed spots, reconstruction of linearly shaped tracks may not be possible. In the case of particles directed nearly perpendicular to the surface, spot-like tracks are obtained (Fig. 3b).

2.4. PNTD– detector preparation and analysis

In this study, plastic nuclear track detectors were used as reference detectors to benchmark the data obtained with the FNTDs. The PNTDs used during the MARE experiment were prepared from Poly-Allyl Diglycol Carbonate (PADC) material manufactured by Track Analysis Systems Ltd under the name TASTRAK. The nominal thickness of the PADC sheets was 0.7 mm and the size of the cut-out detectors measured 32 mm × 18 mm. After exposure the detectors were etched for 12 h in 7N aqueous solution of NaOH at a temperature of 70 °C. The thickness of the removed bulk layer (one side) was 20 μm.

The revealed tracks were examined using a Leitz Metalloplan optical microscope and digital camera. The methodology used in this work for PNTD track analysis is well-established, commonly employed in cosmic-ray and personal dosimetry (Benton, 2004; Benton et al., 1996; Doke et al., 1995; Straube et al., 2010) and used for this purpose also by our group for a long time (Horwacik and Bilski, 2008; Horwacik et al., 2010). The PNTD method is based on the principle that the geometry of the tracks can be described by the ratio of the track etch rate to bulk etch rate ($V=V_T/V_B$) (Henke and Benton, 1971). The etch rate ratio V – which is also a function of the particle's LET – can be determined by measurement of the size of the etched track's opening and thickness of the bulk layer removed during etching. The LET range measured with PNTDs is normally restricted to $LET_{H2O} > 10$ keV/μm.

2.5. NASA Artemis 1 space mission and MARE experiment

The NASA Artemis 1 mission was the first flight of NASA's new programme, which is aimed at returning humans to the Moon and preparing for future deep-space exploration. The mission's main goal was to evaluate the capabilities of the Space Launch System and the Orion spacecraft during an actual mission beyond low Earth orbit. Launched as

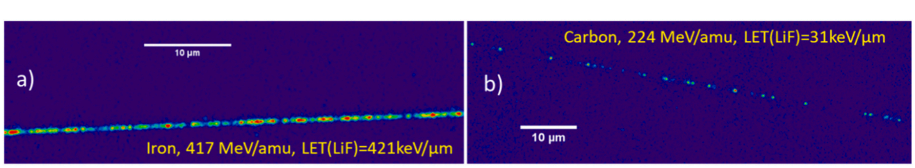

Fig. 1. Illustration showing the effect of ionization density on the structure of fluorescent tracks, using carbon and iron ion tracks as examples. The colour scale is arbitrary. (For interpretation of the references to colour in this figure legend, the reader is referred to the Web version of this article.)

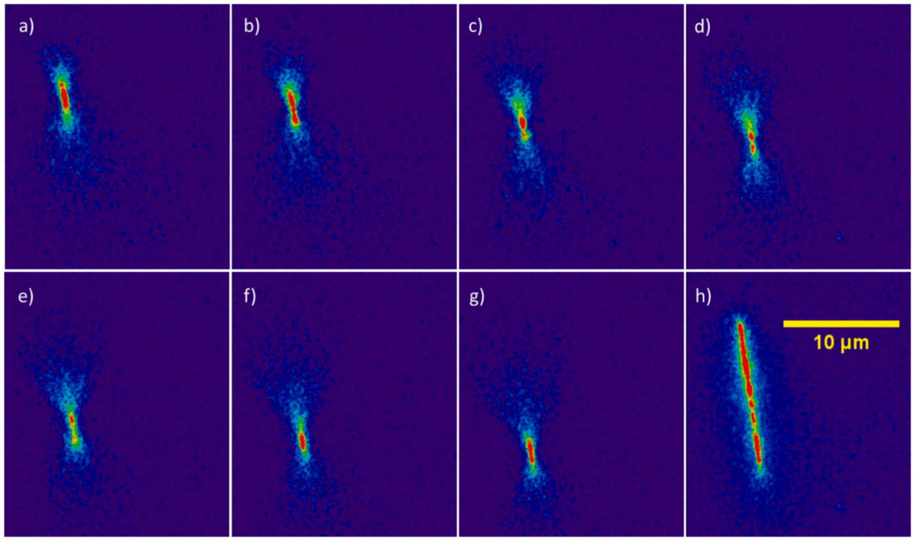

Fig. 2. Track of an iron ion entering the crystal at an angle of incidence of 42°. Panels (a) to (g) show images acquired with the focus set at different depths within the crystal, in steps of 1 μm. Panel (h) shows the maximum intensity projection of all images. The colour scale is arbitrary. (For interpretation of the references to colour in this figure legend, the reader is referred to the Web version of this article.)

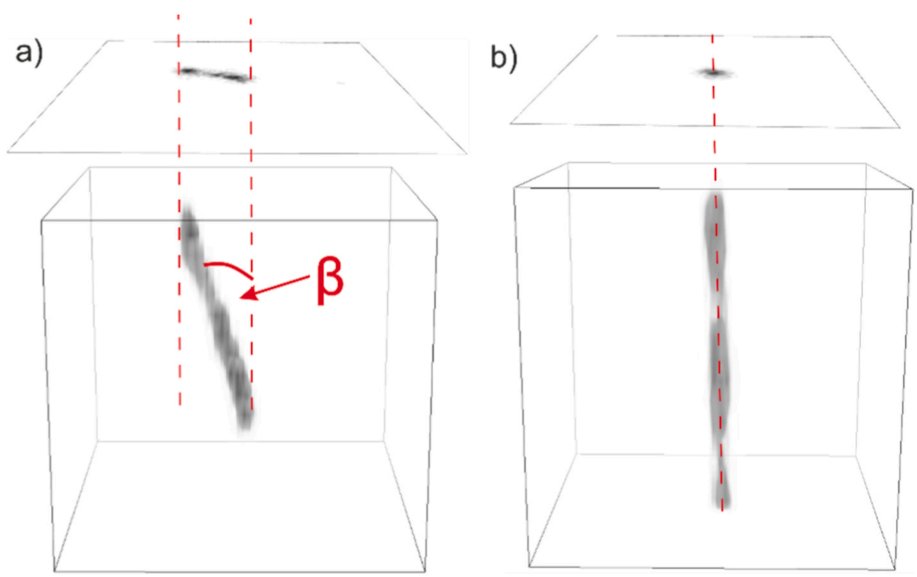

Fig. 3. Schematic illustration of the geometry of fluorescent tracks. a) – a particle directed under an angle of incidence β to the crystal surface, b) – a particle directed perpendicular (β = 0) to the crystal surface. On the upper XY plane: maximum intensity projections.

an uncrewed test flight on 16th November 2022, the Orion capsule followed a complex trajectory during the mission. After launch, the spacecraft travelled towards the Moon and performed a flyby manoeuvre that placed it into a distant retrograde orbit around the Moon. After spending several days in this orbit, the spacecraft performed another lunar flyby and returned to Earth, completing an over 25-day mission on 11th December 2022.

In addition to engineering tests, the spacecraft carried numerous scientific payloads. One of the most important was the MARE, designed to investigate the cosmic radiation exposure that astronauts may experience during lunar missions. MARE was an international project under the scientific leadership of DLR Cologne, Germany, and with the participation of several research groups from various countries. The experiment consisted of exposing two anthropomorphic female phantoms, named Helga and Zohar, equipped with numerous active and passive radiation detectors (Berger, 2023; George et al., 2024) (see Fig. 4). One of the phantoms (Zohar) wore the AstroRad radiation protection vest, intended to provide shielding against low-energy protons as would be seen during a solar particle event.

As part of the MARE experiment, passive detector packages were distributed on both phantoms. The packages were analogous to those used at the International Space Station in the frame of the long-term DOSIS 3D experiment (Berger et al., 2016; Berger, 2025) and contained various detector types provided by different participating research groups. The primary passive dosimetry method relied on thermoluminescent detectors (TLDs) and plastic nuclear track-etched detectors (PNTDs), and LiF FNTDs were placed together with TLDs.

As the present paper is focused on the development of the FNTD measurement methodology, it contains only a small fragment of the MARE passive dosimetry results and the complete report on the results obtained by different participants using various detector systems placed in different locations on the MARE phantoms will follow.

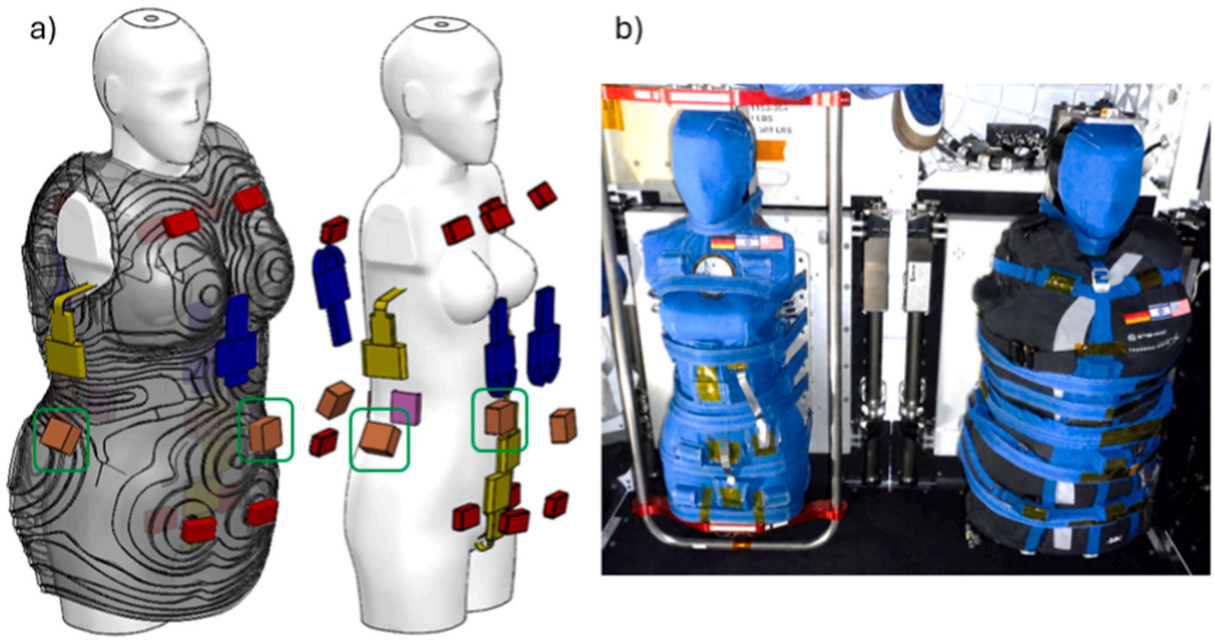

Fig. 4. a) Schematic illustration of the Zohar phantom with and without the AstroRad vest (the passive detector packages encircled with green lines); b) Photo of Helga (left) and Zohar (right) phantoms mounted in the Orion cockpit before launch. Source: DLR, NASA. (For interpretation of the references to colour in this figure legend, the reader is referred to the Web version of this article.)

3. Results and discussion

3.1. Extracting LET data from fluorescent tracks

The general approach to reconstructing an LET spectrum from a nuclear track detector is based on assigning a single LET value to each track (throughout this paper, LET always refers to unrestricted linear energy transfer). This requires the prior establishment of a relationship between some track parameters and LET. In the case of PNTDs, where such an approach has been applied for decades, the relevant parameter is the track etch rate, as mentioned in Section 2.4. Over the last years, considerable effort has been devoted to investigating the correlation between the intensity of fluorescent tracks in LiF FNTDs and the LET of charged particle radiation, by irradiating the detectors with various accelerated ion beams (Bilski et al., 2019, 2024a; Muñoz et al., 2026). This resulted in an unambiguous relationship being established for values of LET in LiF exceeding about 10 keV/μm (which corresponds to LET in water of about 4.5 keV/μm) (Bilski et al., 2024a).

However, most of this work was carried out with ion beams directed perpendicular to the detector surface, while cosmic radiation, obviously, is isotropic. In addition, it was found that the angle of incidence had a significant influence on the fluorescence intensity of a track. This is because a microscope lens focused at a certain depth in the sample can register not only light from that depth, but also some unfocused light from the layers above and below. In the case of tracks directed perpendicular to the surface, this may lead to a significant increase in track intensity. This effect decreases as the angle of incidence increases, and for tracks that are approximately parallel to the surface (i.e. angle of incidence β of about 90°), no effect is present.

It was also observed that the magnitude of this angular effect depends on the LET. This is due to the structure of the tracks. As was discussed in section 2.3, densely ionizing particles, such as iron ions, produce nearly continuous tracks, whereas those characterized by low LET consist of spots that may be separated by many micrometres. In the latter case, the contribution of unfocused light is smaller or even negligible.

Analysis of the fluorescent images created by cosmic radiation therefore requires taking into account the angular dependence and introducing appropriate corrections. The necessary experimental data were extracted from a limited number of irradiations which were carried out with ions directed under different angles. Fig. 5 presents results for two extreme cases, i.e. the ratio of the intensities of nearly perpendicular tracks (spots, $I_{\perp}$) to nearly parallel tracks (lines, $I_{\parallel}$). This ratio, denoted as *R*, may be described by the following empirical formula:

$$R = \frac{I_{\perp}}{I_{\parallel}} = 0.63 \cdot ln(L) - 0.87 \qquad [1]$$

where *L* represents LET_{LiF}. For tracks with LET_{LiF} below about 20 keV/μm (LET_{H2O} = c.a. 9 keV/μm) intensity of parallel and perpendicular tracks are assumed to be equal.

Fig. 6 presents track intensities for all tested angles of incidence, normalized to 90° angle. This plot clearly illustrates the effects of both the angle of incidence and LET on track intensity. To facilitate the use of these data for correcting the measured track intensities, empirical functions described by the formula given in Equation [2] were fitted to the data points.

$$f = \begin{cases} R, \ \beta < 10^{\circ} \\ a \cdot \exp\left(-\frac{\beta}{15^{\circ}}\right) + 1, \ \beta \geq 10^{\circ} \end{cases} \qquad [2]$$

where: β– angle between a track and the surface normal (incidence angle).

Parameter a is defined in relation to *R*:

$$a = (R-1) \Big/ \exp\left(\frac{10^{\circ}}{15^{\circ}}\right) \qquad [3]$$

As was mentioned, most of the calibration irradiations of FNTDs with ion beams were carried out using beams directed perpendicular to the detector surface. A limited number of data gathered with nearly parallel beams were insufficient to establish a meaningful calibration curve. To facilitate obtaining the calibration, formula [1] was used to recalculate the data of the perpendicular tracks to the parallel tracks (Fig. 7). The data were then approximated by an empirical function, described by the following formula, derived using the least-squares minimization:

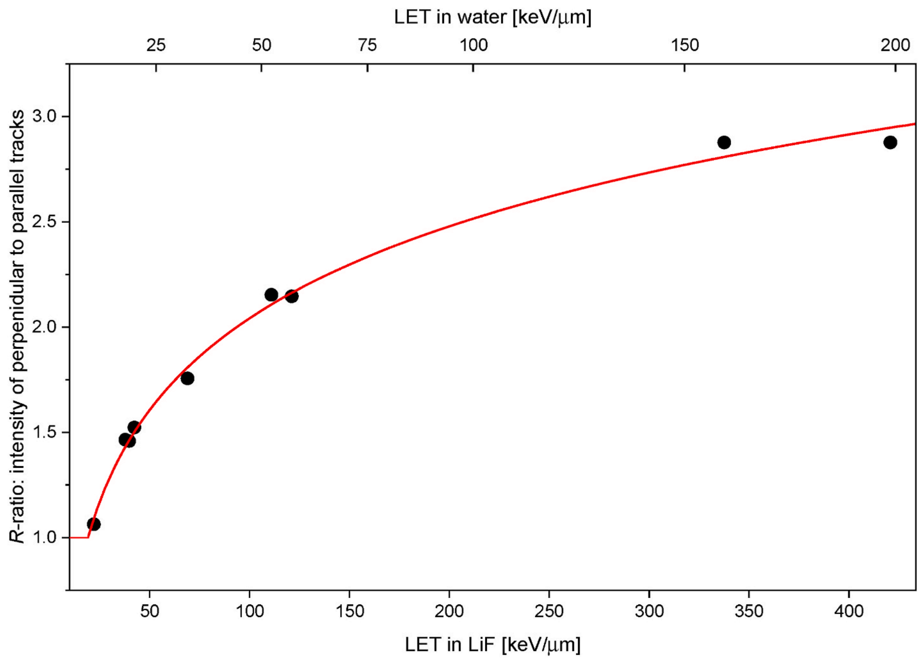

Fig. 5. Dependence of the ratio of intensities of perpendicular and parallel fluorescent tracks registered in LiF on LET.

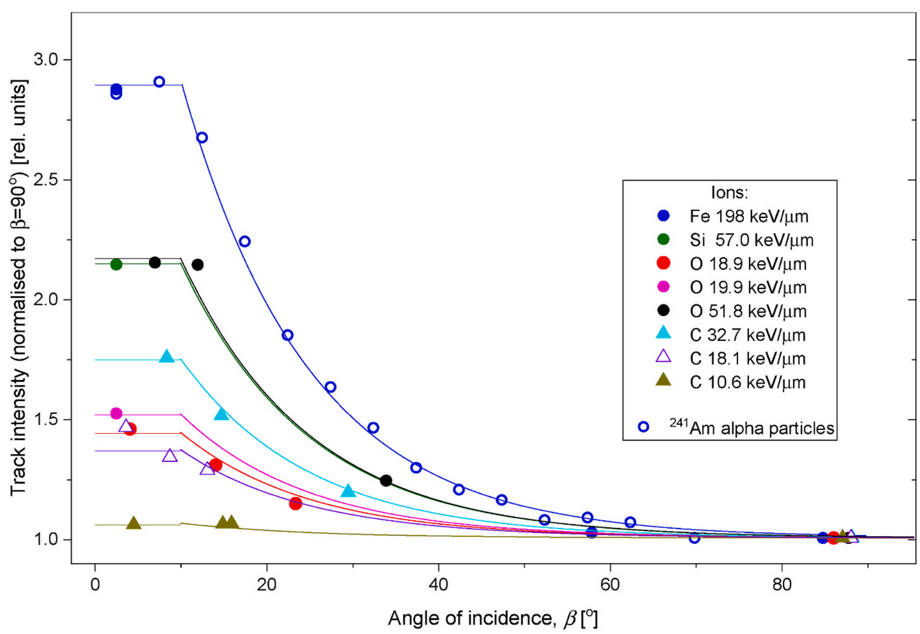

Fig. 6. Relative track intensities measured for various particles and angles of incidence normalized to the values measured for nearly parallel tracks of the respective particles. LET values given in the legend represent LET in water. Lines represent functions described by formula [2], fitted to the experimental data points.

$$I(L) = \begin{cases} 0.85 \cdot L + 32.8, \; L < 15 \, \dfrac{keV}{\mu m} \\ 11.72 \cdot L^{0.50}, \; L \in \left[15, 200\right) \dfrac{keV}{\mu m} \\ 9.45 \cdot L^{0.54}, \; L \geq 200 \dfrac{keV}{\mu m} \end{cases} \quad [4]$$

Assigning LET value to a track requires therefore solving of the following equation with regard to L:

$$I_{meas} = I(L) \cdot f(L, \beta) \quad [5]$$

where I_{meas} – track intensity measured in the image, $I(L)$ – undisturbed track intensity (approximated by formula [4]), $f(L, \beta)$ – correction factor calculated with formula [2], L – LET in LiF. This equation was solved numerically for each track using the Solver add-in for the Excel spreadsheet program.

3.2. Track images of cosmic radiation

Fig. 8 presents several examples of typical track images obtained with LiF FNTDs within the MARE experiment. Panel a) shows a long track of a high-energy heavy ion (in fact, this track is longer, extending beyond the scanned volume of the crystal). Similar long track, but of a lighter particle, is shown in panel d). Panel b) shows products of a

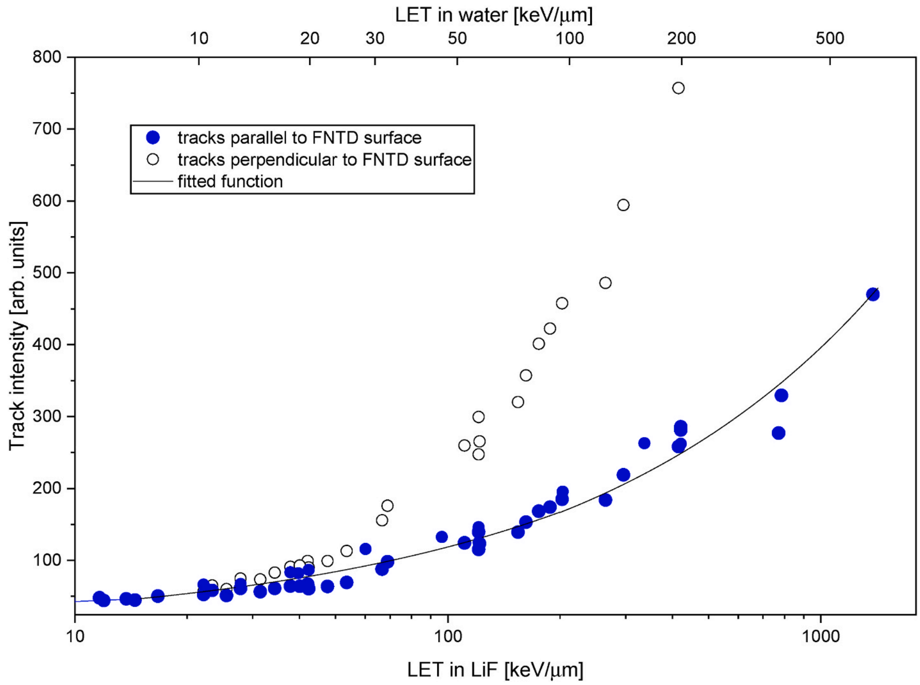

Fig. 7. Relationship between fluorescent track intensity and LET. Solid line represents the function fitted with formula [4].

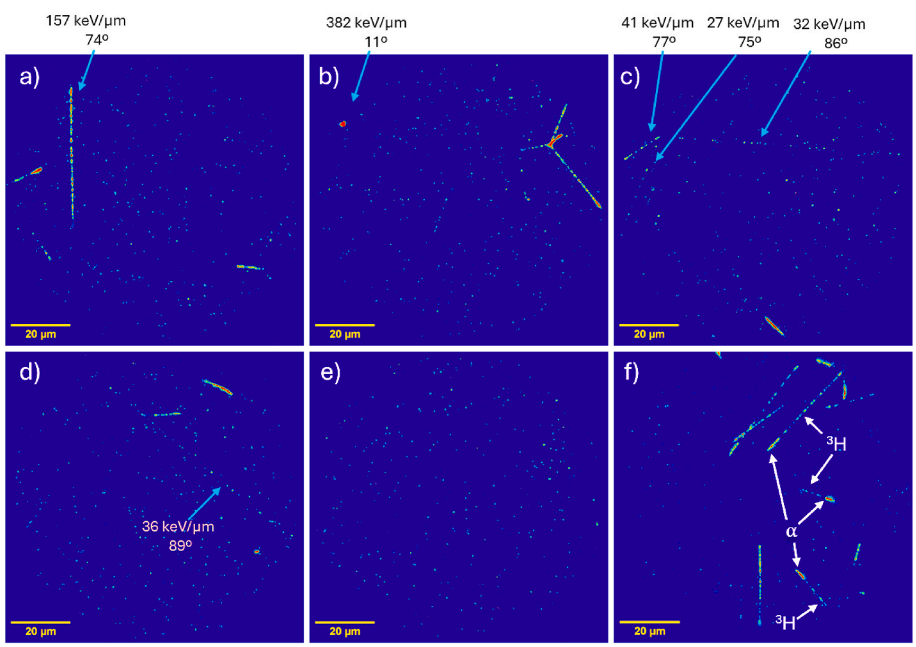

Fig. 8. Examples of typical track images registered with LiF FNTDs within the MARE experiment. Each image is the maximum intensity projection of the stack of 20 single images acquired with 1-μm steps into a crystal. Panels a) to e) represent ^{7}LiF detectors, while panel f) ^{nat}LiF. For the selected tracks the obtained values of LET in water and angle of incidence are given. The colour scale is arbitrary. (For interpretation of the references to colour in this figure legend, the reader is referred to the Web version of this article.)

nuclear reaction involving four particles. On the left side of this panel, there is a very bright spot-like track of a very densely ionizing particle, which was directed nearly perpendicular to the detector surface. Panel c) also shows a nuclear reaction, with three visibly involved particles. In addition to the linearly shaped tracks, in all images, one can see a multitude of dots, which are point-like tracks created by particles of lower LET. In some cases, only such tracks were visible within the scanned volume, as is illustrated in panel e).

All these images were acquired with ^{7}LiF FNTDs, whereas the last panel f) shows an image obtained with ^{nat}LiF detector. One can see in this image several characteristic tracks of the products of the thermal and epithermal neutrons (n,α) reaction with ^{6}Li nuclei. They consist of a short, bright track of an alpha particle and a much longer, but not that bright, track of a tritium nucleus. The presence of these tracks was found to be a very interfering effect. They are indeed quite distinctive, and in terrestrial radiation fields, they stand out from any other tracks or background noise. That makes ^{nat}LiF FNTDs a very good tool e.g. for personal neutron dosimetry. However, in space conditions these tracks can be easily confused with ion tracks. In some cases, when most of a track is well visible (such as in the example presented in Fig. 8f), distinguishing them is possible, but not in a general case, when often only part of a track is present in an image. For that reason, ^{nat}LiF detectors were excluded from analysis aimed at extracting LET data and all further presented results will be based entirely on ^{7}LiF detectors.

For comparison, in Fig. 9 examples of the tracks registered with etched PNTDs are presented. They are mostly of conical shape, with opening circular or elliptical – depending on the particle's angle of incidence.

3.3. LET spectra measured at MARE phantoms

3.3.1. Linear tracks

Fig. 10 shows the distribution of the counted tracks as a function of LET_{H2O}. For the lowest LET_{H2O} values, a decrease in the number of tracks is observed, despite the fact that LiF FNTDs are capable to register particles with LET_{H2O} values down to 4.5 keV/μm, as is shown in Fig. 7. A decrease of the detection efficiency was previously reported for protons (Bilski et al., 2024a), for which an efficiency of only around 25% was found at LET_{H2O} = 4.5 keV/μm (measured for geometry with particle beams directed perpendicularly to the detector surface). Similar results were obtained for high-energy light ions (Muñoz et al., 2026), using a confocal microscope. The detection efficiency was found to be approximately 30% for ^{4}He (5.4 keV/μm) and 50% for both ^{16}O (18.9 keV/μm) and ^{12}C (17.9 keV/μm) ions. This efficiency reduction is most likely due to the structure of low-LET tracks, which consist of just a few sparsely distributed dots (see section 2.3). In most cases, it is not possible to assign these dots to the path of a single particle. Such a series of dots can be recognized as a single track only in specific cases, when they lie nearly horizontally, the distances between dots are small and they are not overlapped by too many other point tracks — hence a deficiency of low-LET tracks in the spectrum. It should also be mentioned, that the acquisition time of a single image was set to 20 s to avoid saturation of high-LET tracks. If the acquisition time were longer, the low-LET tracks would be more clearly visible.

Track distribution, as presented in Fig. 10, provides only a qualitative information about the radiation. To obtain meaningful results, the particle fluence should be calculated. The cosmic radiation fluence is usually defined as the number of particles impinging on a given surface, per unit area and solid angle. For track-etched detectors the differential LET fluence spectra are calculated with the following formula (Benton, 2004; Doke et al., 1995):

$$\frac{d\Phi}{dL} = \left(2\pi A\,cos^{2}\delta_{C}\right)^{-1}\frac{dN}{dL} \qquad [6]$$

where Φ – fluence, A – area of the analysed surface, N – number of tracks, δ_C – critical angle (measured between track and the detector surface, $\delta = 90°-\beta$) for track registration, L – LET in water. In the case of FNTDs there is no critical angle ($\delta_C = 0$), therefore the formula simplifies to:

$$\frac{d\Phi}{dL} = (2\pi A)^{-1}\frac{dN}{dL} \qquad [7]$$

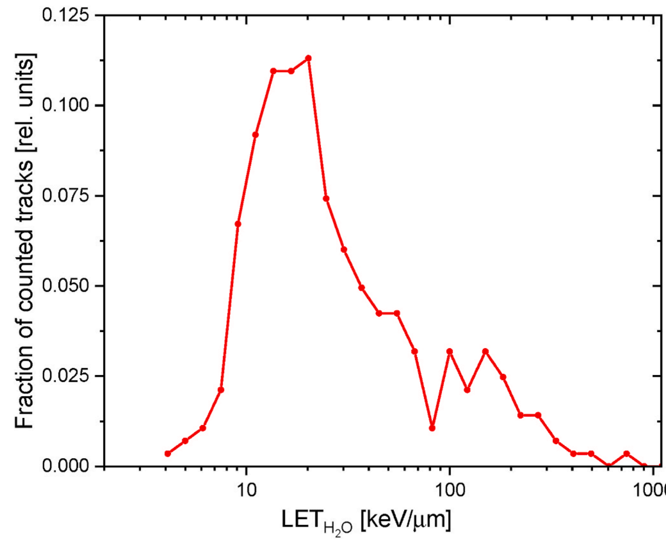

Fig. 10. Histogram of linearly shaped fluorescent tracks (sum of all tracks counted in the analysed volume, detector location at the Zohar phantom, under the vest) as function of LET in water. Total number of counted tracks: 283.

Calculation of the fluence according to the described formalism requires counting only particles crossing a defined surface. In the case of FNTDs, this means counting only tracks within a single layer of a stack; for PNTDs, this is ensured by the nature of the etching process. To improve the track statistics, the data for selected layers (typically layers 2 to 6) were counted separately and then averaged. Deeper layers were excluded from the count as it was observed that the number of visible tracks decreases with depth, likely due to attenuation of the luminescent light. Similarly, there were fewer tracks in the first layer, which may be interpreted as a border effect.

Fig. 11 presents the fluence spectra calculated in the described way for the detectors located on the left side of the Zohar phantom, under and over the vest, compared with analogous spectra measured with PNTDs. In general, the shape of both spectra is similar, however FNTD data clearly show significant fluctuations around the PNTD-measured spectra. This seems to be attributable to the much lower total number of counted tracks: about 150 for FNTDs, and nearly 2000 for PNTDs. Below 15-20 keV/μm, the FNTDs seem to underestimate the fluence, which is caused by the discussed above point-like shape of the low-LET tracks. Above about 100 keV/μm, the fluence measured by FNTDs is systematically higher than that measured by PNTDs. This might be again partly explained by the low statistics or by the inaccurate calibration curve in the high-LET region, which is based on a few data points. On the other hand, one may speculate that a more fundamental factor may also be at play. LiF FNTDs contain lithium nuclei, which are absent in PNTDs. When hit by a high-energy neutron, a light Li nucleus may gain sufficient kinetic energy to be moved by several micrometres or more, which would be registered as a track. High-energy neutrons are present in a space vehicle's radiation environment due to the nuclear interactions of primary protons and heavy ions with matter. For example, a 20 MeV

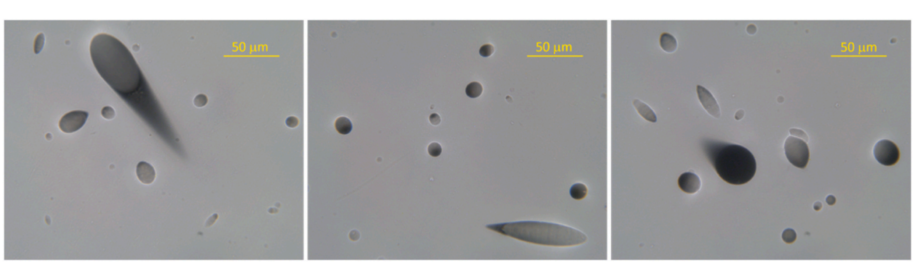

Fig. 9. Examples of the cosmic ray tracks registered with PADC PNTDs.

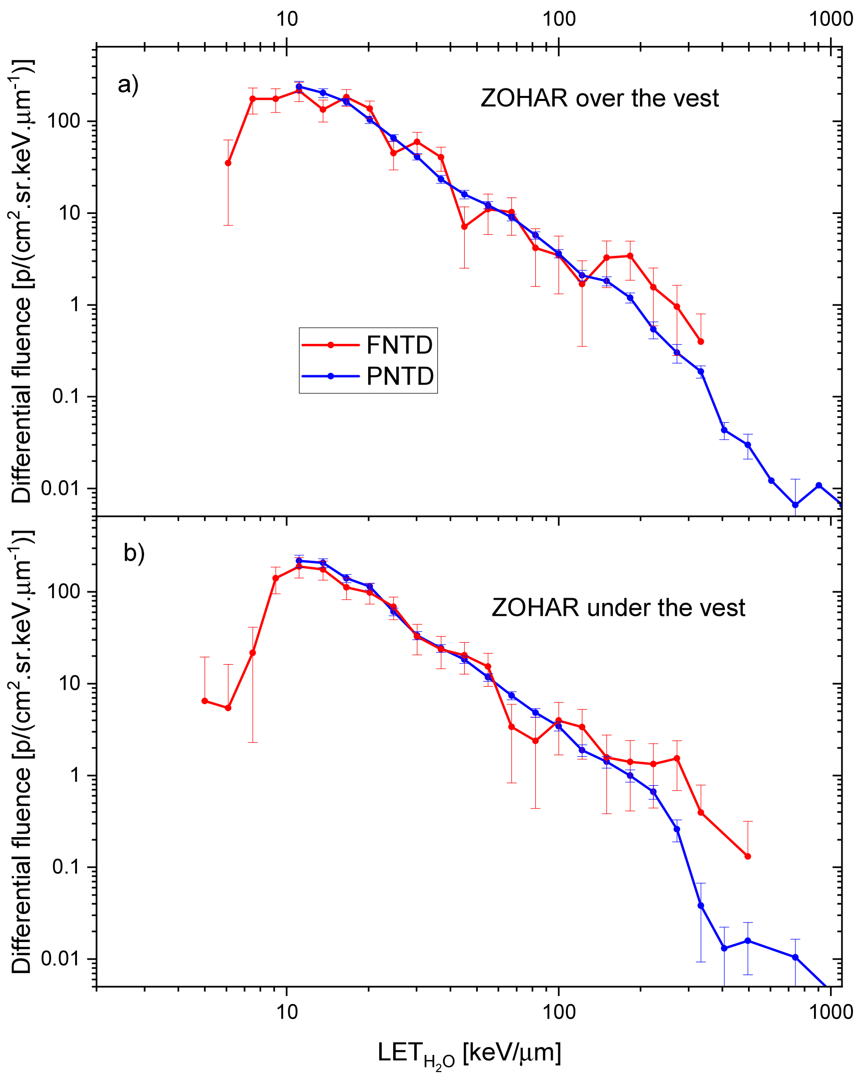

Fig. 11. Comparison of the differential LET fluence spectra measured with LiF FNTD and PNTD. Detector's location at the Zohar phantom: a) over the vest, b) under the vest. The error bars represent only counting statistics (1 SD).

neutron can impart a maximum energy of about 8.8 MeV to a Li nucleus (the amount of energy depends on the scattering angle). Such a particle would have a range of about 16 μm in LiF and an LET_{H2O} of 200 keV/μm.

Knowing the differential LET fluence spectra it is possible to calculate dose (D), dose equivalent (H) and quality factor (Q) of the radiation, using the following formulas:

$$D = \frac{4\pi \times 1.602 \times 10^{-9}}{\rho} \sum_i L(i)N(i) \quad [8]$$

$$H = \frac{4\pi \times 1.602 \times 10^{-9}}{\rho} \sum_i L(i)N(i)Q(i) \quad [9]$$

$$Q = \frac{H}{D} \quad [10]$$

$Q_i(L)$ values were derived according to ICRP Publication No. 60 (ICRP, 1991).

The results of such calculations are presented in Table 1. The results from FNTD systematically show higher values than those from PNTD. This is caused by the discussed overestimation of the high-LET part of the spectrum (L > 100 keV/μm), which has a significant impact on dose and quality factor. When calculations were restricted to LET_{H2O} values below 100 keV/μm, the agreement was within 15% for dose and within a few percent for quality factor.

Table 1
Dose in water, quality factor and dose equivalent measured with FNTD and PNTD on Zohar phantom. The given uncertainties represent only counting statistics (1SD) and do not include contributions connected to calibrations, corrections etc.

Position	Detector type	LET_{H2O} > 10 keV/μm			10 keV/μm < LET_{H2O} < 100 keV/μm		
		D [mGy]	Q	H [mSv]	D [mGy]	Q	H [mSv]
over the vest	LiF FNTD	3.4 ± 0.5	15.7 ± 3.5	54.1 ± 9.5	1.8 ± 0.2	10.1 ± 1.9	17.7 ± 3.0
	PADC PNTD	2.9 ± 0.1	13.6 ± 0.7	39.0 ± 1.4	1.7 ± 0.1	10.4 ± 0.5	18.0 ± 0.6
under the vest	LiF FNTD	3.1 ± 0.5	15.5 ± 3.8	48.5 ± 9.3	1.4 ± 0.2	9.3 ± 2.0	13.4 ± 2.5
	PADC PNTD	2.4 ± 0.1	13.7 ± 2.1	32.7 ± 1.3	1.6 ± 0.1	10.1 ± 0.5	16.6 ± 0.7

3.3.2. Point tracks

The data discussed so far comprised only linearly shaped tracks. This leaves out a large number of point-like tracks, which are prevalent in every image acquired with FNTDs exposed in space. As mentioned previously, this type of track originates from low-LET particles. Therefore, analysing them could potentially provide information on LET, which could help reduce the tendency to underestimate the spectrum below about 20 keV/μm. However, this task is very challenging. Firstly, the relationship between the number of point tracks and the particle fluence is unclear (it is evident that the number of point tracks is greater than the number of particles). Secondly, the calibration provided by formula [4] is invalid in this instance. The approach that worked well for linear tracks was based on the maximum track intensity. The intensity of a point track, which is only a small part of a longer, unidentified track, is generally obviously lower than the maximum, but the relation between them is unknown. Nevertheless, we have conducted a preliminary investigation to recognise the problem.

The images were analysed using the "*Analyse Particles*" command of ImageJ software, which provided data on the number of point tracks and the intensity of each of them. To avoid counting artifacts, only tracks with the area exceeding 5 pixels were counted. Fig. 12 presents the obtained in this way distribution of point tracks as function of track intensity.

In order to utilize the calibration in accordance with equation [4], which was the only available calibration, it was necessary to establish a correlation between the average intensity of point tracks and the maximum track intensity. In the absence of experimental data concerning this relationship, it was decided to use an arbitrary factor by which the track intensities would be multiplied. Fig. 13 shows the outcome of such an operation with the multiplication factor of 1.6, which was chosen as producing the best agreement with the PNTD data. It should be emphasized that these results should obviously be treated as merely indicative of the potential embedded in this data, not as a 'real' result of measurement. For such results to be considered meaningful, they would need to be obtained by proper calibration, for which a method has yet to be developed. Nevertheless, if such a method could be developed, combining data from linear and point tracks could make it possible to reconstruct the fluence spectrum over a wider LET range than is possible with PNTD detectors.

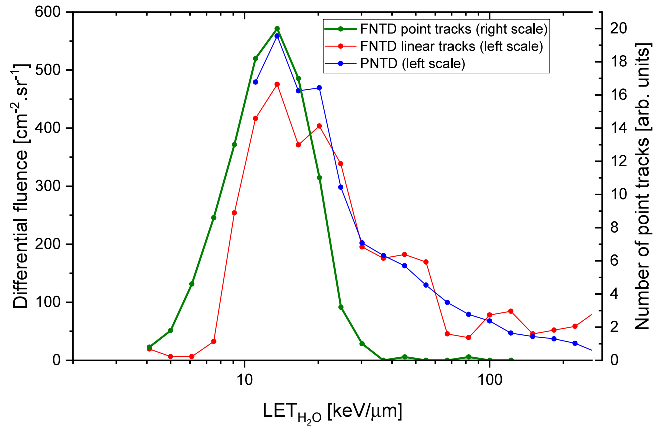

Fig. 13. Histogram of the intensity of point tracks compared with the differential fluence LET spectra measured with FNTDs and PNTDs (detectors location at the Zohar phantom, under the vest). Average intensity of point tracks was arbitrary assumed to be 1.6 times lower than the maximum intensity of a track.

4. Conclusions

In this study, we developed a method to reconstruct LET fluence spectra of a complex cosmic radiation field using parameters of fluorescent tracks and then applied this method to analyse results from FNTD detectors exposed in lunar orbit as part of the MARE experiment. The satisfactory agreement between the FNTD data and the spectra measured using classic, track-etched detectors, obtained despite the low counting statistics, is an encouraging result that confirms the correctness of the proposed approach. The observed overestimation of the radiation quality factor (by about 15%) and the dose (by up to 30%) is due to the overestimation of the spectrum for $LET_{H2O} > 100$ keV/μm, which may be caused by the presence of the recoil lithium nuclei. When dose and quality factor calculations were restricted to LET_{H2O} values below 100 keV/μm, the agreement was within 15% for dose and within a few percent for quality factor.

Future work will include an attempt to develop a method to analyse point-like, low-LET tracks, which could expand the LET range of the measured spectrum. We also plan to develop an automated microscope scanning system to enable effective scanning of the entire FNTD surface.

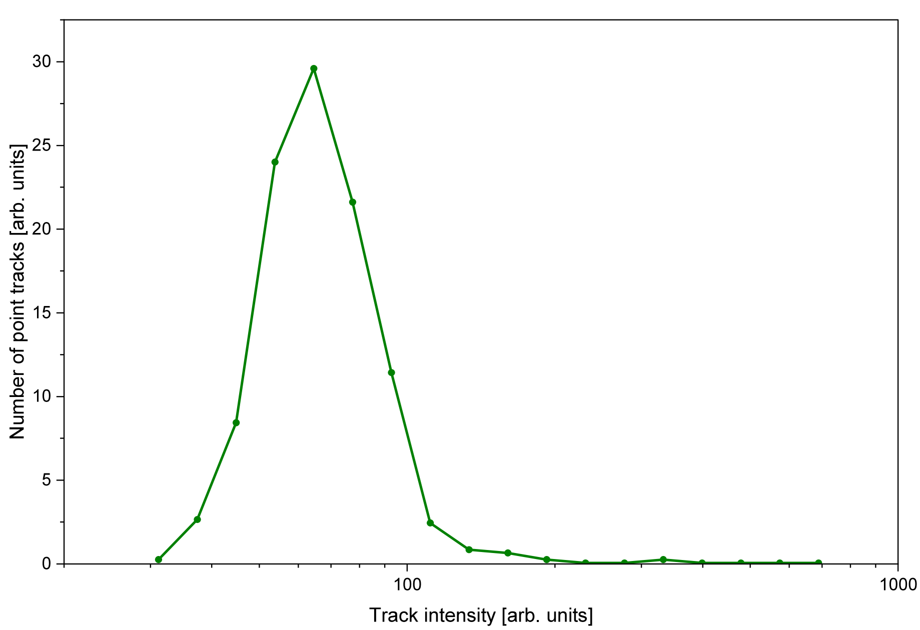

Fig. 12. Histogram of point tracks (FNTD location at the Zohar phantom, under the vest) as function of track intensity.

Work on fine-tuning the calibration curves by irradiating FNTDs with various ion beams will also continue.

CRediT authorship contribution statement

P. Bilski: Writing – original draft, Methodology, Investigation, Funding acquisition, Formal analysis, Conceptualization. **A. Kilian:** Writing – review & editing, Software, Methodology, Investigation. **M. Sankowska:** Writing – review & editing, Methodology, Investigation. **T. Horwacik:** Writing – review & editing, Investigation. **T. Berger:** Writing – review & editing, Resources.

Declaration of competing interest

The authors declare that they have no known competing financial interests or personal relationships that could have appeared to influence the work reported in this paper. P. Bilski is Senior Associate Editor for this journal and was not involved in the editorial review or the decision to publish this article.

Acknowledgments

This work was funded by the National Science Centre, Poland (Grant No 2020/39/B/ST9/00459). We gratefully acknowledge the opportunity to perform an intercomparison of heavy ion responses for PNTD and FNTD detectors within the DOSIS 3D project as part of a research project at the Heavy Ion Medical Accelerator (HIMAC) at NIRS/QST, Chiba, Japan and are grateful for the steady support of our colleagues at NIRS/QST, namely Satoshi Kodaira and Hisashi Kitamura. We are also very grateful to Ivan Muñoz (German Cancer Research Center, DKFZ, Heidelberg, Germany) for FNTD irradiations carried out at the Heidelberg Ion-Beam Therapy Center (HIT).

Data availability

Data will be made available on request.

References

Akselrod, G.M., Akselrod, M.S., Benton, E.R., Yasuda, N., 2006. A novel Al_2O_3 fluorescent nuclear track detector for heavy charged particles and neutrons. Nucl. Instrum. Methods B 247, 295–306. https://doi.org/10.1016/j.nimb.2006.01.056.

Akselrod, M., Kouwenberg, J., 2018. Fluorescent nuclear track detectors – review of past, present and future of the technology. Radiat. Meas. 117, 35–51. https://doi.org/10.1016/j.radmeas.2018.07.005.

Akselrod, M.S., Sykora, G.J., 2011. Fluorescent nuclear track detector technology - a new way to do passive solid state dosimetry. Radiat. Meas. 46, 1671–1679. https://doi.org/10.1016/j.radmeas.2011.06.018.

Benton, E., 2004. Radiation Dosimetry at Aviation Altitudes and in Low-Earth Orbit. National University of Ireland, Dublin. PhD Thesis.

Benton, E.R., Benton, E.V., 2001. Space radiation dosimetry in low-Earth orbit and beyond. Nucl. Instrum. Methods Phys. Res. B 184, 255–294. https://doi.org/10.1016/S0168-583X(01)00748-0.

Benton, E.V., Frank, A.L., Csige, I., Frigo, L.A., Benton, E.R., 1996. LET spectra measurements on LDEF: variations with shielding and location. Radiat. Meas. 26, 783–791. https://doi.org/10.1016/S1350-4487(96)00085-6.

Berger, T., 2023. NASA Artemis I mission and the MARE experiment, 26th workshop on radiation monitoring for international space station (WRMISS). Rome, Italy. https://wrmiss.org/workshops/twentysixth/Berger_MARE.pdf.

Berger, T., 2025. DOSIS and DOSIS 3D – active and Passive Radiation Measurements in Columbus from 2009 – 2025. 28th Workshop on Radiation Monitoring for International Space Station (WRMISS) Cologne. https://wrmiss.org/workshops/twentyeighth/.

Berger, T., Przybyla, B., Matthiä, D., et al., 2016. Dosis & DOSIS 3D: long-term dose monitoring onboard the Columbus Laboratory of the International Space Station (ISS). J. Space Weather Space Clim. 6, A39. https://doi.org/10.1051/swsc/2016034.

Bilski, P., Marczewska, B., 2017. Fluorescent detection of single tracks of alpha particles using lithium fluoride crystals. Nucl. Instrum. Methods B 392, 41–45. https://doi.org/10.1016/j.nimb.2016.12.003.

Bilski, P., Marczewska, B., Gieszczyk, W., Kłosowski, M., Naruszewicz, M., Sankowska, M., Kodaira, S., 2019. Fluorescent imaging of heavy charged particle tracks with LiF single crystals. J. Lumin. 213, 82–87. https://doi.org/10.1016/j.jlumin.2019.05.007.

Bilski, P., Marczewska, B., Sankowska, M., Gieszczyk, W., Mietelski, J.W., 2020. Range-based method of alpha-particle spectrometry using LiF fluorescent nuclear track detectors. Measurement 160, 107837. https://doi.org/10.1016/j.measurement.2020.107837.

Bilski, P., Marczewska, B., Sankowska, M., Kilian, A., Swakoń, J., Siketić, Z., Olko, P., 2024a. Detection of proton tracks with LiF fluorescent nuclear track detectors. Radiat. Meas. 173, 107083. https://doi.org/10.1016/j.radmeas.2024.107083.

Bilski, P., Matthiä, D., Berger, T., Gaza, R., 2024b. Calculation of relative luminescent efficiency of TL/OSL detectors to cosmic radiation spectrum in cis-lunar space. Radiat. Meas. 177, 107264. https://doi.org/10.1016/j.radmeas.2024.107264.

Doke, T., Hayashi, T., Nagaoka, S., Ogura, K., Takeuchi, R., 1995. Estimation of dose equivalent in STS-47 by a combination of TLDs and CR-39. Radiat. Meas. 24, 75–82. https://doi.org/10.1016/1350-4487(94)00084-E.

George, S.P., Gaza, R., Matthiä, D., et al., 2024. Space radiation measurements during the Artemis I lunar mission. Nature 634, 48–52. https://doi.org/10.1038/s41586-024-07927-7.

Henke, R.P., Benton, E.V., 1971. On geometry of tracks in dielectric nuclear track detectors. Nucl. Instrum. Methods 97, 483–489. https://doi.org/10.1016/0029-554X(71)90250-3.

Horwacik, T., Bilski, P., 2008. INP Kraków passive detectors. In: Uchihori, Y., Benton, E. (Eds.), Results from the ICCHIBAN-3 and ICCHIBAN-4 Experiments to Intercompare the Response of Space Radiation Dosimeters,Chiba, pp. 162–181.

Horwacik, T., Bilski, P., Körner, C., Facius, R., Berger, T., Nowak, T., Reitz, G., Olko, P., 2010. Determination of Nuclear Tracks Parameters on Sequentially Etched PADC Detectors, 38th COSPAR Assembly. Bremen, Germany. https://www.cospar-assembly.org/abstractcd/OLD/COSPAR-10/abstracts/data/pdf/abstracts/F24-0043-10.pdf.

ICRP, 1991. 1990 Recommendations of the International Commission on Radiological Protection, No. 60. Publication.

Kilian, A., Bilski, P., Sankowska, M., 2025. Background Remover – an effective tool for processing noisy microscopy images. J. Microsc. 300, 77–93. https://doi.org/10.1111/jmi.70002.

Muñoz, I.D., Sankowska, M., Kilian, A., Jäkel, O., Bilski, P., 2026. Characterization of lithium fluoride fluorescent nuclear track detectors for linear energy transfer measurements in light-ion beams using confocal microscopy. Radiat. Meas. 192, 107623. https://doi.org/10.1016/j.radmeas.2026.107623.

Sankowska, M., Bilski, P., Kłosowski, M., Kilian, A., Gieszczyk, W., Marczewska, B., 2024. Isotopically enriched lithium fluoride crystals for detection of neutrons with the fluorescent track technique. Materials 17. https://doi.org/10.3390/ma17205029.

Schindelin, J., Arganda-Carreras, I., Frise, E., et al., 2012. Fiji: an open-source platform for biological-image analysis. Nat. Methods 9, 676. https://doi.org/10.1038/nmeth.2019.

Straube, U., Berger, T., Reitz, G., Facius, R., Fuglesang, C., Reiter, T., Damann, V., Tognini, M., 2010. Operational radiation protection for astronauts and cosmonauts and correlated activities of ESA Medical Operations. Acta Astronaut. 66, 963–973. https://doi.org/10.1016/j.actaastro.2009.10.004.